Two-phase swirling flow and gas hydrate particle deposition behavior in bending pipelines

processes

MDPI

Article

Two-Phase Swirling Flow and Gas Hydrate Particle Deposition Behavior in Bending Pipelines

Yongchao Rao [1,2], Long Zheng [1,2], Shuli Wang [1,2,*], Wenjing Wu [1,2], Zijia Gong [1,2], Shidong Zhou [1,2] and Chuang Wen [3,*]

[1] Jiangsu Key Laboratory of Oil-Gas & New-Energy and Transportation Technology, Changzhou University, Changzhou 213164, China
[2] School of Petroleum and Gas Engineering, Changzhou University, Changzhou 213164, China
[3] School of the Built Environment, University of Reading, Reading RG6 6AH, UK
* Correspondence: wsl@cczu.edu.cn (S.W.); c.wen@reading.ac.uk (C.W.)

Abstract: The present study employs numerical simulation to analyze the behavior of gas hydrate particles in bending pipelines, focusing on the influence of swirl flow on particle deposition under varying bending angles, pipe-to-diameter ratios, Reynolds numbers, and twist rates. Results indicate that larger bending angles, smaller twist rates, and higher Reynolds numbers produce stronger swirl flows at pipe entry and sustain higher swirl numbers along the pipeline. Conversely, larger pipe-to-diameter ratios result in greater swirl number variations, slower attenuation, and weaker outflow. Moreover, the phenomenon of hydrate particle deposition is more serious in the straight pipe section. Particle retention at the pipe outlet is 1.5 times higher than in the bending section. The bent pipe is more conducive to the flow of particles. For instance, with a bend rate increasing from 1 to 4, the swirl number decreases by 57.49%. Additionally, the deposition rate of particles is reduced at higher Reynolds numbers, with rates falling below 1% at a Reynolds number of 20,000. These findings highlight the need to optimize swirl flow parameters to reduce hydrate deposition, preventing blockages and improving pipeline safety in industrial applications.

Keywords: gas hydrate; swirl flow; twisted tape; deposition law; two-phase fluid flow

Academic Editor: Ali Hassanpour

Received: 30 December 2024
Revised: 21 February 2025
Accepted: 27 February 2025
Published: 3 March 2025

Citation: Rao, Y.; Zheng, L.; Wang, S.; Wu, W.; Gong, Z.; Zhou, S.; Wen, C. Two-Phase Swirling Flow and Gas Hydrate Particle Deposition Behavior in Bending Pipelines. *Processes* **2025**, *13*, 725. https://doi.org/10.3390/pr13030725

1. Introduction

Natural gas, as a vital clean energy source, is extensively utilized across various sectors of the global economy. The primary modes of natural gas transportation currently include pipeline delivery, liquefied natural gas (LNG) transport, and compressed natural gas (CNG) transport [1,2], with pipeline delivery being the dominant method. Approximately 70% of the world's oil and 90% of its natural gas are transported via pipelines on land. Among the various factors impacting the safety of oil and gas pipelines, hydrate plugging is one of the most prevalent issues. Natural gas hydrates are clathrate crystalline compounds with an ice-like structure, formed under high pressure and low temperature [3,4].

During the transportation of natural gas through pipelines, factors such as high-velocity gas flow, low-temperature and high-pressure pulsations, and specific structural configurations significantly influence hydrate formation. These conditions facilitate the generation and accumulation of hydrates, particularly in areas such as pipe bends and low points. As the accumulated hydrates grow, the volume fraction of hydrates in the pipeline gradually increases, eventually exceeding the critical threshold that the gas flow can effectively transport. This results in severe fluctuations in pipeline transport pressure.

Furthermore, particle adhesion, both between particles and with the pipe wall, leads to continuous binding, aggregation, and deposition, progressively blocking the pipeline with hydrates [5]. The formation and accumulation of gas hydrates within pipelines not only cause blockages in pipes and valves, reducing gas transport capacity, but also pose significant safety risks, such as pipeline damage and rupture.

In recent years, two innovative approaches have emerged based on the concept of natural gas hydrate risk management: Low Dosage Hydrate Inhibitors (LDHIs) and spiral flow methods [6]. The primary mechanism by which LDHIs control hydrate formation involves inhibiting the growth and aggregation of natural gas hydrate particles, differing fundamentally from the suppression mechanism of traditional thermodynamic inhibitors that modify hydrate formation conditions. LDHIs are mainly classified into two categories: kinetic inhibitors and anti-agglomerants. Kinetic inhibitors prevent the growth of natural gas hydrate nuclei, while anti-agglomerants hinder the aggregation of hydrate particles. Kinetic inhibitors are typically used in gas-dominated pipelines, whereas anti-agglomerants require the presence of an oil phase for effectiveness [7,8]. Due to their relatively low dosage requirements, LDHIs show promising potential for widespread application.

Pipeline spiral flow hydrate control technology, proposed by the hydrate research group at Changzhou University [9], represents a significant departure from chemical inhibition methods. This technique leverages the carrying capacity of spiral flow to enable the safe transportation of hydrates at higher concentrations. Unlike non-spiral flow, spiral flow introduces a tangential velocity component perpendicular to the axial flow direction. This tangential velocity enhances the transport of hydrate particles, increasing the volume fraction of hydrates in transit and reducing particle deposition [10,11]. Additionally, spiral flow increases the shear forces between the fluid and the pipe wall, as well as between particles, improving hydrate flowability and reducing particle aggregation.

During the transportation of hydrate slurry through pipelines, it is critical to avoid regions where the volume fraction of hydrate slurry causes a rapid increase in pressure drop. In bending pipeline structures, particles transitioning from horizontal straight sections to bends exhibit distinct movement behaviors due to density differences between liquid and solid phases. This phase separation causes particles to migrate toward the outer wall of the bend, significantly increasing particle concentration in this region. Near the bend exit, particle concentration on the outer wall peaks, leading to hydrate accumulation and an increase in the volume fraction of hydrate particles. Consequently, controlling the inlet volume fraction alone is insufficient to prevent hydrate-related issues in bending pipelines. A comprehensive investigation into the factors affecting the maximum concentration of hydrate particles in bending pipes is essential.

In the field of multiphase flow in bending pipes, particularly regarding particle transportation, extensive research has been conducted domestically and internationally. Al-Obaidi [12] studied the effects of flow structure variations, such as velocity magnitude and radial velocity profiles, under different configurations. Using the Taguchi method (TM) for experimental design, they optimized differential pressure values concerning shaft diameter. Xu [13] utilized a microfluidic device to focus on macroscopic phenomena, though lacking visualization and temporal resolution. Their results indicated that hydrate formation in microfluidic chips required phase equilibrium and perturbations in regions with crystal nuclei, with perturbations in random pore structures proving most effective. Sun [14] controlled water-gas flow rates to study two-phase flow in hydrate sediments, identifying three stages of hydrate re-formation: induction, mass agglomeration, and pore gas consumption. Using magnetic resonance imaging (MRI), Sun [15] observed the hydrate re-formation process, confirming its role in plugging during water-gas flow. Further studies by Sun [16] explored dissociation modes combining water-gas flow and depressurization, demonstrating that

higher water-gas flow rates and lower dissociation pressures enhanced energy recovery and reduced energy input.

Wu et al. [17] investigated naphthalene deposit migration in gas pipelines, analyzing transport patterns in various configurations, including horizontal bends. They examined factors such as particle size, gas flow velocity, temperature, and pressure. Lv et al. [18] used simulations to study large particle solid-liquid flow in U-shaped bends, identifying the influence of secondary flows on particle distribution. Gao et al. [19] employed particle image velocimetry (PIV) to measure gas-water-sand three-phase flow in combined bends, discovering that centrifugal forces caused particles to migrate outward, while gravity hindered flow in ascending sections.

Bending pipes are critical components of long-distance pipelines, and understanding hydrate particle flow behavior in bends is essential for optimizing pipeline design. Such studies can improve the efficiency and safety of pipeline gas transmission. Currently, research on spiral particle flow in gas pipelines has predominantly focused on straight pipes, with limited attention to hydrate particle flow in bending sections [20]. In the present study, we investigate the influence of spiral flow twist rates on hydrate particle deposition within bending pipelines using computational fluid dynamics (CFD) simulations. A finite volume method-based CFD model is employed to simulate hydrate slurry flow and analyze the deposition process. Key factors such as bend diameter ratios and flow parameters are systematically examined to understand their impact on hydrate particle accumulation and concentration. This research provides insights into optimizing spiral flow techniques for mitigating hydrate deposition and ensuring safe and stable pipeline operations. Novel contributions include the evaluation of spiral flow effectiveness in bending pipeline sections, the identification of critical deposition patterns, and recommendations for pipeline design improvements to enhance natural gas transportation efficiency and safety.

2. Methodologies

Figure 1 describes the flowchart for the present study. The process begins with setting the twisted tape parameters and defining the working conditions. Grid-independent verification and model validation are then conducted. If the model validation is successful, the study proceeds to analyze the change in swirl numbers, discuss the residence time distribution of hydrate particles, and calculate the residual distribution of hydrate particles. Next, hydrate particle deposition laws are determined, and the deposition rate parameters are updated. If the calculation converges, the process finishes; otherwise, the process iterates by adjusting parameters. The system control and optimization are useful for this modeling study as suggested in the references [21,22]. If the model validation fails, the process returns to the previous time step for re-evaluation.

2.1. Physical Model

The pipeline's physical model was designed using SolidWorks (SOLIDWORKS2021 SP0-SP5), featuring an internal diameter of 25 mm. It consists of straight pipes in the front and rear sections, with a 90° bend in the middle. This pipeline configuration is depicted in Figure 2. The bend rate is the rate of the bending radius R to the bending diameter D, and the bend rate is from 1 to 4. A helical strip, acting as a vortex generator, is installed at the pipeline inlet and extends 0.5 m in length. The helical strip design includes three different twist ratios (Y), defined as the ratio of one full 360° turn's length (H) to the strip's width (D). These ratios are 6.2, 7.4, and 8.8. The strip design incorporates wall thickness considerations to ensure accurate simulation of the gas-solid two-phase flow within the pipeline. The computational domain is divided into two segments: the region containing the helical strip and the flow domain formed between the strip and the pipe's inner wall. A structured grid

partitioning method is applied to the helical strip to achieve high mesh quality, efficient computation, and high calculation accuracy. For the flow domain, where the geometric structure is more complex due to the presence of the helical strip, an unstructured grid is utilized to accommodate the intricate geometry. While this method requires higher computational resources, it ensures better adaptability. The details can be found in our previous studies [23].

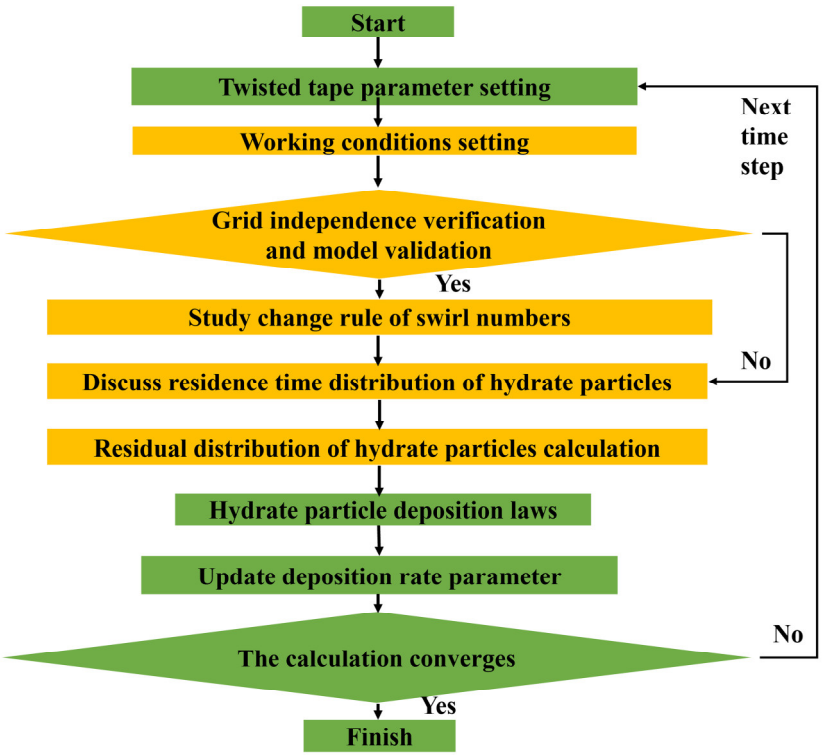

Figure 1. Flowchart for the present study.

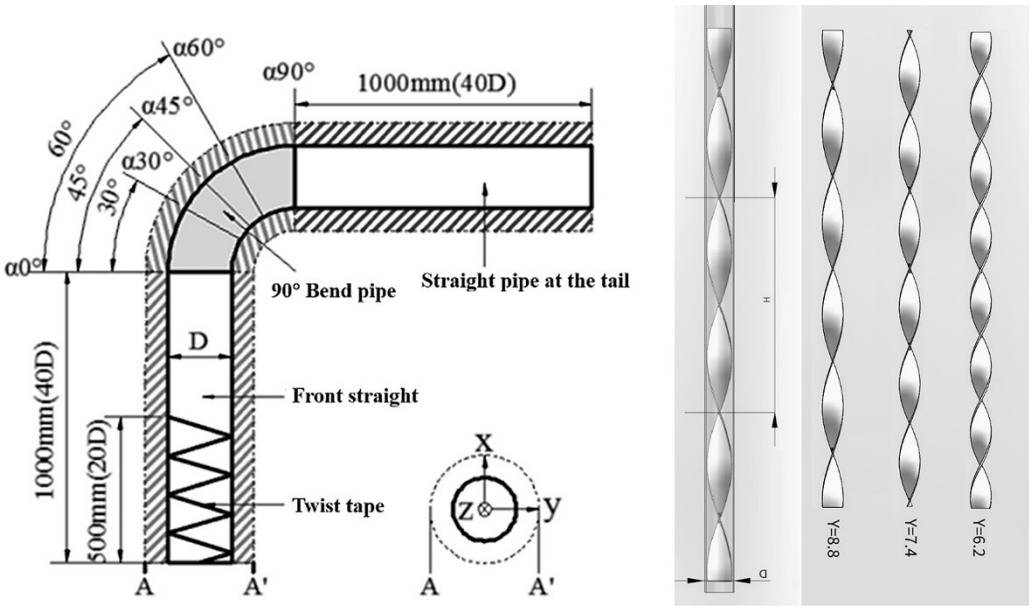

Figure 2. Pipeline system for the numerical simulation of gas hydrate flows (Reprinted from Rao et al. [23], an open-access article from Springer Nature).

2.2. Boundary Conditions and Physical Properties

At the inlet, a velocity inlet condition is specified. The gas phase consists of natural gas, while the solid phase comprises hydrate particles with a mass flow rate of 10^{-6} kg/s. Hydrate particles are continuously generated at the inlet. To enable comparative analysis, Reynolds numbers (Re) of 5000, 10,000, and 20,000 are used at the inlet, and these Reynolds numbers correspond to the actual engineering data. The outlet boundary is set to a pressure outlet, and a no-slip condition is applied to the walls, accounting for gravitational effects.

This study focuses on simulating the flow and deposition behavior of gas-solid two-phase flow influenced by the swirl flow generated by the helical strip. Methane (CH_4) is selected as the gas-phase medium, while the solid phase consists of natural gas hydrate particles, modeled as homogeneous spheres with uniform size. Table 1 outlines the key physical property parameters, including gas-phase density (ρ_g), solid-phase density (ρ_s), and gas-phase dynamic viscosity (μ_g). All parameters are configured under standard conditions.

Table 1. Basic parameters table.

ρ_g/(kg·m^{-3})	ρ_s/(kg·m^{-3})	μ_g/(μPa·s)	Average Particle Size (mm)
0.717	650	11.067	0.06

2.3. Mathematical Model

2.3.1. Governing Equations

Continuity equation,

$$\frac{\partial \rho}{\partial t} + \frac{\partial}{\partial x_i}(\rho u_i) = 0 \tag{1}$$

Momentum equation,

$$\frac{\partial}{\partial t}(\rho u_i) + \frac{\partial}{\partial x_j}(\rho u_i u_j) + \frac{\partial P}{\partial x_i} - \frac{\partial \tau_{ij}}{\partial x_j} - \frac{\partial \tau_{ij}^{-1}}{\partial x_j} = 0 \tag{2}$$

where ρ is gas density, u is velocity, p is static pressure, τ_{ij} is viscous stress tensor, and t is time.

2.3.2. Equation of Turbulent Flows

The RNG $k-\varepsilon$ model is adopted for turbulence simulation. Compared to the $k-\varepsilon$ model, the RNG variant demonstrates superior performance in flow fields characterized by rotations, bends, and vortices. It also provides enhanced accuracy for flows with high strain rates and pronounced streamwise curvature, such as spiral patterns in swirl-dominated flow regimes.

The governing equations for the $k-\varepsilon$ model are applied as follows:

$$\frac{\partial}{\partial t}(\rho k) + \frac{\partial}{\partial x_i}(\rho k u_i) = \frac{\partial}{\partial x_j}\left(\alpha_k \mu_{eff} \frac{\partial k}{\partial x_j}\right) + G_k + G_b - \rho\varepsilon - Y_M + S_k \tag{3}$$

$$\frac{\partial}{\partial t}(\rho \varepsilon) + \frac{\partial}{\partial x_i}(\rho \varepsilon u_i) = \frac{\partial}{\partial x_j}\left(\alpha_\varepsilon \mu_{eff} \frac{\partial \varepsilon}{\partial x_j}\right) + C_{1\varepsilon}\frac{\varepsilon}{k}(G_k + C_{3\varepsilon}G_b) - C_{2\varepsilon}\rho\frac{\varepsilon^2}{k} - R_\varepsilon + S_\varepsilon \tag{4}$$

$$R = \frac{C_\mu \rho \eta^3 \left(1 - \frac{\eta}{\eta_0}\right)\varepsilon^2}{1 + \beta\eta^3}\,\frac{\varepsilon^2}{k} \tag{5}$$

$$\left|\frac{\alpha-1.3929}{\alpha_0-1.3929}\right|^{0.6321}\left|\frac{\alpha+2.3929}{\alpha_0+2.3929}\right|^{0.3679}=\frac{\mu_{mol}}{\mu_{eff}} \tag{6}$$

where $\eta=\frac{S_k}{\varepsilon}$, $\eta_0\approx 4.38$, $\beta=0.012$, $\alpha_0=1$.

The μ_{eff} is effective viscosity, equations as follows:

$$d\left(\frac{\rho^2 k}{\sqrt{\varepsilon\mu}}\right)=1.72\frac{v}{\sqrt{v^3-1+C_v}}dv \tag{7}$$

where $C_v\approx 100$, $v=\frac{\mu_{eff}}{\mu}$.

2.3.3. Discrete Phase Model

The gas-solid two-phase spiral flow was simulated using the Discrete Phase Model (DPM), which is grounded in the Eulerian-Lagrangian approach. In this framework, the fluid phase is treated as a continuous medium, while the solid particles are modeled as discrete entities. The overall flow field distribution is obtained by solving the Navier-Stokes equations, incorporating the coupling interactions between the fluid and the particles. Through this coupling, the trajectories of a defined number of particles are tracked, and their behavior is described within the Eulerian coordinate system. The discrete phase typically assumes a low concentration of solid particles, generally below 10%, ensuring the validity of the DPM in dilute flow conditions.

In a suspended state, the forces acting on particles in the fluid reach equilibrium. The equation governing the motion of the particles can be expressed as follows:

$$m_i\frac{du_i}{dt}=\left(\sum F\right)_i \tag{8}$$

where, m_i is the mass of particles, kg; u_i is Particle velocity, μPa·s; $\left(\sum F\right)_i$ is The combined force on the particles.

In the flow, particles are influenced by several forces, including the added mass force, inertial force, gravitational force, pressure gradient force, drag force, buoyancy force, and the Saffman lift force. Among these, the added mass force arises from the acceleration of the fluid displaced by the particles. Based on the principles of ideal (inviscid) fluid dynamics, the mass generating this force is equivalent to half the mass of the fluid displaced by the solid particles during motion. Consequently, the added mass force can be expressed as follows:

$$F_{vm}=-\frac{2}{3}\pi r^3\rho\left(\frac{dv_p}{dt}-\frac{dv}{dt}\right) \tag{9}$$

where F_{vm} is additional mass force, kg·m/s^2; r is pipe radius, m; ρ is gas density, kg/m^3; t is time, s.

Inertial force arises when an object undergoes acceleration. The inertia of the object resists changes to its state of motion, maintaining its original velocity or position. This resistance manifests as a force acting in the direction opposite to the applied force, commonly referred to as inertial force, and can be mathematically expressed as

$$F_i=-\frac{4}{3}\pi r^3\rho_p\frac{du_p}{dt} \tag{10}$$

where F_i is inertial force, kg·m/s^2.

As solid particles move, they are subjected to their own gravitational force. In the simulation, where hydrate particles are modeled as uniform spheres, this gravitational force can be represented as follows:

$$G = \frac{4}{3}\pi r^3 \rho_p g \tag{11}$$

where G is the gravitational force, kg·m/s^2.

Solid particles in the pipe flow experience a pressure gradient along the flow direction, subjecting them to a corresponding force. This force, known as the pressure gradient force, can be expressed as

$$F_P = -\frac{4}{3}\pi r^3 \frac{dp}{dx} \tag{12}$$

where F_p is pressure gradient force, kg·m/s^2.

The force exerted by a fluid on a solid with relative velocity is referred to as the drag force. The drag force is influenced by various complex factors, making it challenging to describe with a fixed formula. To address this, the concept of the drag coefficient is introduced, expressed as follows:

$$C_D = \frac{F_r}{\pi r^2 \left[\frac{1}{2}\rho (v - v_p)^2\right]} \tag{13}$$

where C_D is the trailing force coefficient.

Therefore, the trailing force can be expressed as the following equation:

$$F_r = \frac{1}{2} C_D \pi r^2 \rho |v - v_p| (v - v_p) \tag{14}$$

where F_r is trailing force, kg·m/s^2.

Buoyancy refers to the net force arising from the pressure difference exerted by a fluid on the surfaces of an object submerged in it. This force can be expressed as

$$F_a = \frac{4}{3}\pi r^3 \rho g \tag{15}$$

where F_a is Buoyancy, kg·m/s^2.

Saffman lift refers to the lift force generated when there is a velocity difference between a particle and the surrounding fluid, accompanied by a velocity gradient in the fluid that is perpendicular to the particle's motion. This lift results from the variation in velocity across the particle, transitioning from low to high speed. However, in turbulent flows, its magnitude is often negligible. This force can be expressed as

$$F_s = 1.61(\mu\rho)^{\frac{1}{2}} d^2 (v - v_p) \left|\frac{\partial v}{\partial y}\right|^{\frac{1}{2}} \tag{16}$$

where F_s is Saffman force, kg·m/s^2.

2.4. Calculation Methods

In the calculations, a discrete phase model (DPM) is employed, utilizing a pressure-based implicit solver to perform transient simulations of gas-solid, two-phase, three-dimensional swirl flows in natural gas hydrate pipelines. The turbulence model adopted is the RNG k-ε model, which extends the conventional k-ε model by incorporating an additional term into the ε equation. This enhancement improves the model's adaptability to rotating flow fields, leading to higher accuracy in computational results.

The particle motion is modeled using the Discrete Phase Model, which allows for the adjustment of particle properties, velocity, and mass flow rate through parameter settings. A second-order upwind interpolation scheme is applied to calculate the momentum components, turbulent kinetic energy components, and dissipation rates with second-order accuracy. Pressure-velocity coupling is achieved using the SIMPLEC algorithm. Convergence is considered achieved when the absolute residuals drop below 1×10^{-6}, signifying the completion of the computation.

2.5. Grid Independence Verification

To verify grid independence, this study utilized three different mesh sizes: 600,000, 800,000, and 1,000,000 elements. In the simulations, all parameter settings remained identical except for the mesh density. The velocity distribution at the center of the cross-section, located 8D downstream from the inlet, was selected for comparison. The velocity comparison chart shows that all three mesh groups exhibit similar trends in velocity variation, indicating consistency in the simulation results. However, with a mesh size of 600,000 elements, the velocity variation displays relatively larger errors compared to the other two cases, suggesting insufficient precision and lower data reliability. Conversely, the results from the 800,000 and 1,000,000 element meshes demonstrate minimal discrepancies. Nonetheless, the computational time required for the 1,000,000-element mesh is significantly longer than for the 800,000-element mesh. Considering the balance between computational efficiency and result accuracy, a mesh count of 800,000 elements is deemed most appropriate for the calculations. The details can be found in our previous studies [23].

2.6. Model Validation

To validate the reliability of the model, an experimental setup was constructed using a pipeline with a length of 1.2 m and an inner diameter of 25 mm. Colored sand particles with a diameter of 0.06 mm were used as substitutes for hydrate particles, flowing through the pipeline alongside the gas. The experiment was conducted under ambient temperature and pressure conditions. The experimental results were compared with the simulation data, the experimental and simulation results exhibit small errors across the range of Reynolds numbers tested, demonstrating strong agreement. These findings confirm that the model is suitable for simulating the transport of natural gas containing hydrate particles. The details can be found in our previous studies [23].

3. Results and Discussion

Numerical simulations were conducted to study the swirl flow attenuation and the deposition behavior of hydrate particles during their transportation in bending pipe sections, considering various factors such as bending pipe angles, pipe diameter ratios, Reynolds numbers, and twist rates. The study primarily focused on the variations in swirl number, residence time, concentration distribution, and the deposition patterns of hydrate particles, with the aim of extending the safe transportation distance. This research holds significant importance for ensuring the safety and reliability of the pipeline.

3.1. The Change Rule of Swirl Numbers

The swirl number is a critical physical quantity that characterizes the flow dynamics of swirl flows and serves as an essential parameter for assessing their strength. It is defined as the ratio of dimensionless tangential momentum to axial momentum represented mathematically as

$$s = \frac{\int_0^R \rho u w r dA}{R\int_0^R \rho u^2 dA} = \frac{\int_0^R \rho u w r d(\pi r^2)}{R\int_0^R \rho u^2 d(\pi r^2)} = \frac{w}{u} \quad (17)$$

where R is the inner diameter of the pipe, ρ is the density of the fluid, u is the axial velocity of the fluid, w is the tangential velocity of the fluid, A is the cross-sectional area of the swirling pipe, and the speed is considered to be the average time velocity. This relationship encapsulates the interplay between the tangential and axial momentum components, providing insight into the rotational behavior of the fluid within the pipeline.

Figure 3 illustrates the variation in swirl number at three distinct positions: the inlet, middle, and outlet, for bending pipes with different angles, under identical flow conditions. The data indicate that the swirl number at the inlet increases with the bend angle. Specifically, a larger bending angle results in a higher swirl number upon entry, signifying a stronger initial swirl intensity. This trend can be attributed to the geometric influence of the bend, which amplifies the tangential velocity component as the angle increases. However, as the fluid progresses through the bending pipe, the swirl number decreases continuously. This decay is a consequence of energy dissipation due to viscous effects and turbulence. Despite this attenuation, the swirl number at any given position remains higher for pipes with larger bending angles, confirming that more pronounced bends sustain stronger swirl flows. The observed behavior highlights the intricate relationship between the geometric configuration of the pipe and the swirl dynamics, where larger angles enhance initial swirl intensity but also experience greater energy loss as the fluid traverses the bend.

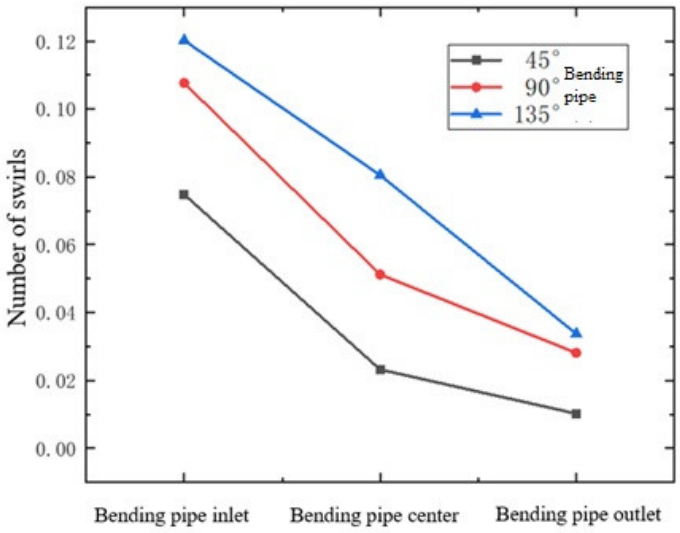

Figure 3. Variation of swirl number under different bending pipe angles.

Table 2 provides a detailed analysis of swirl numbers at various positions for bending pipes with different diameter ratios. The data reveal that the swirl number consistently decreases as the fluid flows through the pipe. Additionally, the rate of change in the swirl number is influenced by the diameter ratio of the pipe. Larger diameter ratios correspond to greater total changes in swirl number over the length of the pipe. To quantify the decay characteristics, the change in swirl number per unit length ($\Delta S/L$) was calculated. The results indicate that (a) for a diameter ratio of 1, the swirl number drops by 57.49%, with a unit-length change of 1.061; (b) for a diameter ratio of 2, the corresponding decrease is 41.15%, with a unit-length change of 0.710; and (c) for a diameter ratio of 4, the swirl number reduces by 31.05%, with a unit-length change of 0.451. This analysis demonstrates that larger diameter ratios result in slower swirl number decay per unit length. The extended pipe sections associated with higher diameter ratios allow for a more gradual attenuation of swirl intensity, although the outflow swirl strength is comparatively weaker. These findings are crucial for optimizing pipe design to maintain desired swirl flow characteristics over extended distances.

Figure 4 illustrates the effect of different twisted rates on the swirl number at various positions along the bending pipe. The twisted rate, defined as the degree of rotation imparted to the flow, significantly influences the initial and sustained swirl characteristics. We found that a smaller twisted rate leads to a higher initial swirl number at the pipe's inlet. This effect arises from the stronger coupling between the tangential and axial velocity components, which enhances the rotational momentum of the flow. Also, as the fluid progresses, the swirl number at corresponding positions remains higher for smaller twisted rates. This behavior underscores the ability of low twisted rates to sustain swirl intensity over longer distances, minimizing energy dissipation. These findings suggest that adjusting the twisted rate can serve as an effective control mechanism for regulating swirl flow behavior. Applications requiring prolonged swirl flow strength can benefit from lower twisted rates, while higher rates may be more suitable for rapid dissipation scenarios.

Table 2. Statistics of swirl number and the variation of swirl number at different positions with different rates of bending pipe diameter.

Bending Pipe-to-Diameter Rate	Bending Pipe Inlet	30° Alpha.	45° Alpha.	60° Alpha.	Bending Pipe Outlet	Δs	Unit Length Δs
1	0.1224	0.1144	0.1014	0.0929	0.0825	0.0399	1.061
2	0.1301	0.1021	0.0912	0.0858	0.0766	0.0535	0.710
4	0.1356	0.1221	0.1089	0.0867	0.06767	0.0679	0.451

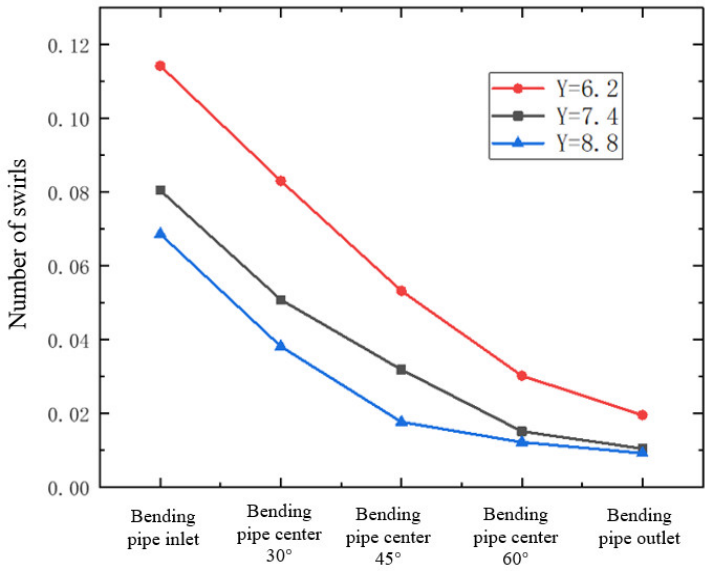

Figure 4. Variation of swirl number under different twisted rates.

Figure 5 presents the variation of the swirl number at different positions under varying Reynolds number conditions. The Reynolds number, a dimensionless parameter representing the ratio of inertial forces to viscous forces, plays a pivotal role in determining flow behavior. The results reveal that higher Reynolds numbers correspond to larger swirl numbers at the pipe's inlet. This correlation can be attributed to the increased flow velocity associated with higher Reynolds numbers, which enhances the tangential velocity component and, consequently, the swirl number. At any given position within the bending pipe, higher Reynolds numbers consistently result in larger swirl numbers. This behavior indicates that increased flow velocity not only strengthens the initial swirl intensity but also aids in maintaining swirl strength over the pipe's length. The influence of the Reynolds number highlights the importance of flow velocity in preserving swirl dynamics. Higher

velocities generate greater momentum, which counteracts the dissipative effects of viscosity and turbulence, thereby prolonging the lifespan of the swirl flow.

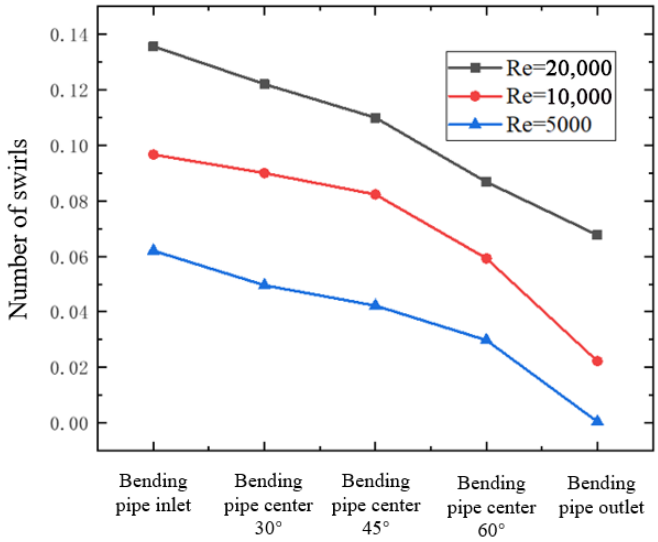

Figure 5. Variation of swirl number under different Re.

3.2. Residence Time Distribution of Hydrate Particles

The residence time distribution (RTD) of hydrate particles in a pipeline is a critical factor in evaluating flow dynamics, particle deposition, and the overall safety of gas hydrate transportation systems. As depicted in Figure 6, the RTD after stable flow is analyzed for a 90° bending pipe under a twisted rate of 6.2 and a Reynolds number of 10,000. The unit of residence time is seconds. The figure provides valuable insights into how hydrate particles behave in a swirling flow and how their residence time varies across different pipeline sections. Upon entering the bending pipe, hydrate particles experience strong swirl flow due to the influence of the twisted band and the high Reynolds number. The twisting mechanism imparts a tangential velocity component to the particles, enhancing their swirl motion and distributing them more uniformly across the cross-section of the pipe. At this stage, the residence time of the particles is relatively short because the swirling motion minimizes localized stagnation and reduces particle retention. This flow behavior is advantageous for mitigating deposition risks at the pipe's entrance.

As the particles progress through the bending section, the intensity of the swirl flow gradually decreases due to resistance forces, including wall friction and viscous dissipation. The curvature of the 90° bend introduces a centrifugal force that pushes the particles toward the outer wall of the pipe. Simultaneously, gravitational forces act on the particles, particularly those with higher mass, causing a redistribution of hydrate particles within the pipe. The combined effects of these forces alter the velocity profile and extend the residence time of the particles as they navigate through the bend. At the exit of the bending pipe, the swirl flow is further weakened, leading to the dissipation of the tangential velocity component. Without the stabilizing effect of the twisted band, the swirling motion diminishes, and the particles begin to accumulate in regions of lower flow velocity. The residence time at this stage increases significantly—more than 1.5 times compared to that at the pipe's bend. This prolonged residence time is a result of reduced axial momentum and the gradual decay of swirling motion. The extended residence time of hydrate particles at the exit of the bending pipe has critical implications for pipeline safety. The slower flow velocity and weakened swirl contribute to particle deposition, particularly along the bottom surface of the pipe, where gravity and centrifugal forces dominate. This deposition not only reduces the effective cross-sectional area of the pipe but also poses risks of blockages

and flow assurance issues in long-term operations. Therefore, the RTD highlights the importance of understanding how pipeline design, such as bend angle and twisted rate, influences particle behavior and deposition tendencies.

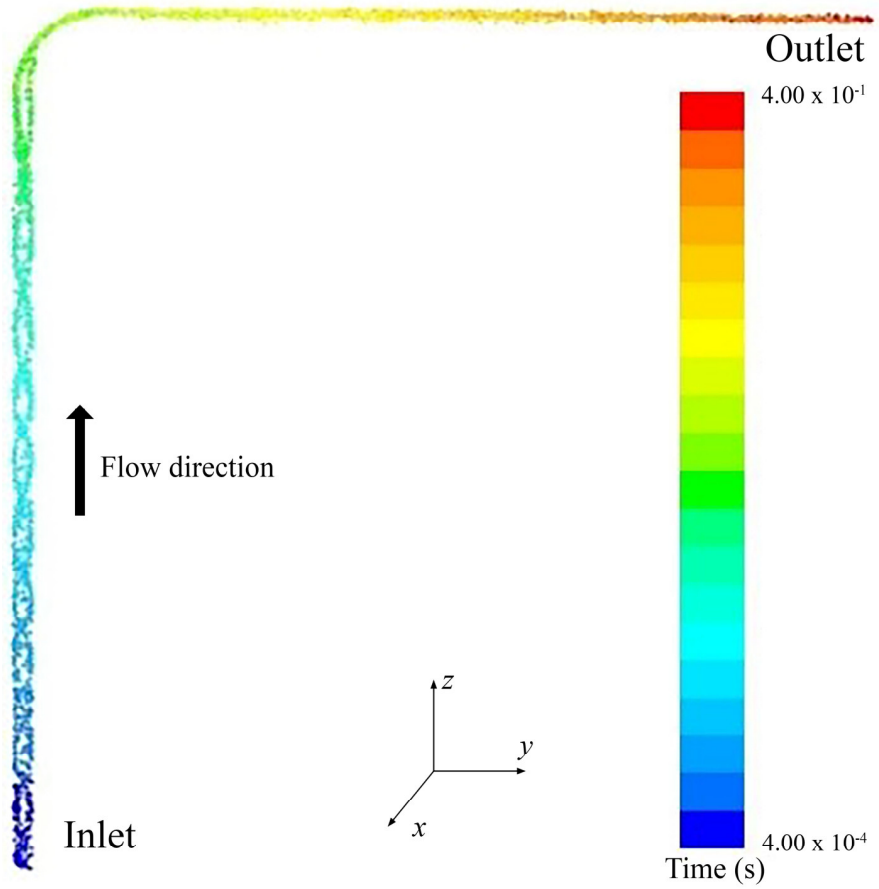

Figure 6. Residual time distribution of hydrate particles.

3.3. Residual Distribution of Hydrate Particles

The residual distribution of hydrate particles within pipelines is a key parameter that determines flow efficiency and operational safety, particularly in bending pipelines where complex interactions between centrifugal forces, gravity, and swirl flow occur. Figures 6–9 provide comprehensive insights into the dynamics of hydrate particle distribution under varying conditions, including high flow rates, swirl flow intensity, and twisted belt configurations. This section delves deeper into the observed phenomena, focusing on the interplay of forces that influence the mass concentration of particles across different pipeline segments.

As shown in Figure 7, the distribution of hydrate particles upon entry into the bending pipe demonstrates a distinct pattern. Under high flow rates and strong swirl flow, the particles are predominantly concentrated near the pipe walls, while the central region exhibits relatively low mass concentration. This distribution arises due to the tangential and axial velocity components of swirl flow. The tangential velocity induces a rotational motion, dispersing the particles uniformly across the cross-section, while the axial velocity propels the fluid forward, maintaining a dynamic equilibrium. This swirl-induced suspension mechanism is particularly effective at preventing particle deposition in the straight sections of the pipeline. The particles remain in suspension due to the strong carrying capacity of the fluid, which minimizes the likelihood of clogging or accumulation near the pipe walls. The entry conditions thus play a pivotal role in ensuring the uniform dispersion of hydrate particles, enhancing transport efficiency.

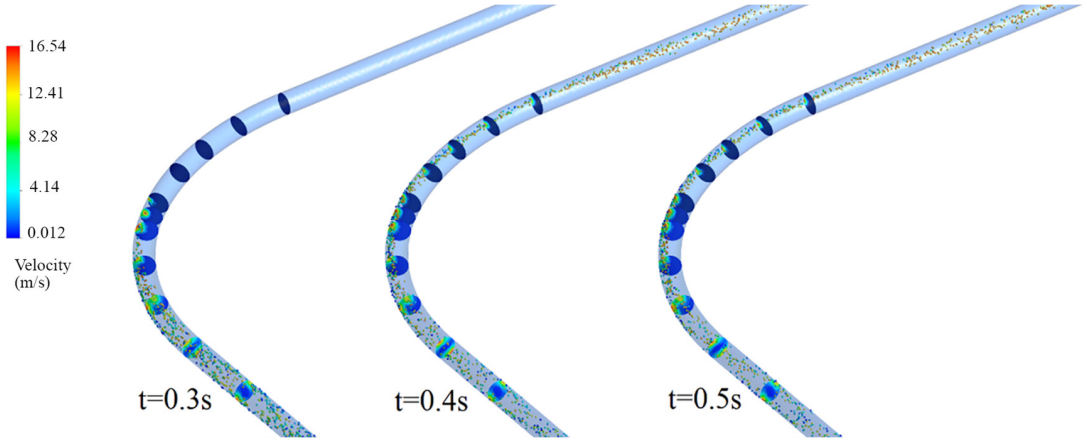

Figure 7. Distribution of particle position and mass concentration in each section of the elbow at different times.

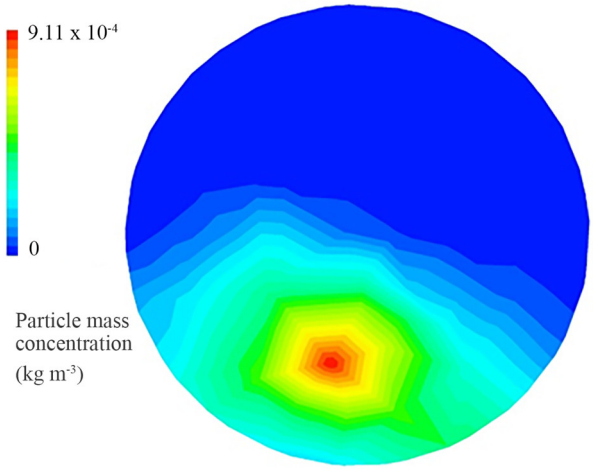

Figure 8. Distribution of particle mass concentration at the exit of the pipe.

When hydrate particles enter the bending pipe, the interaction of centrifugal force and swirl flow significantly alters their distribution. The centrifugal force, acting perpendicular to the pipe curvature, pushes the particles toward the upper outer wall of the bend. Simultaneously, the tangential velocity imparted by the swirl flow continues to rotate the particles, resulting in a dynamic redistribution along the pipe's cross-section. At this stage, the high-speed fluid carries the particles forward, and their concentration near the outer wall increases. However, as the flow progresses, the intensity of the swirl flow diminishes due to viscous dissipation and energy loss. The weakening of tangential velocity causes a gradual attenuation of the swirling motion, allowing gravity to dominate. This transition marks a critical phase in the bending section, where the particles begin to migrate downward, forming localized areas of higher concentration.

Figure 8 illustrates the distribution of particle mass concentration at the exit of the bending pipe. After exiting the bending section, the particles, influenced by gravity, are concentrated near the lower part of the pipe. The swirling motion, which had previously maintained particle suspension, has now largely dissipated, allowing gravity to exert a stronger influence. The exit flow dynamics reveal that, under high flow rates, most hydrate particles are successfully carried out of the pipe along with the fluid. However, regions with lower velocity or turbulence intensity may experience localized particle deposition. This residual accumulation, though limited under high flow conditions, poses a greater risk in pipelines operating at medium or low flow rates, where the reduced carrying capacity of the fluid may result in particle buildup.

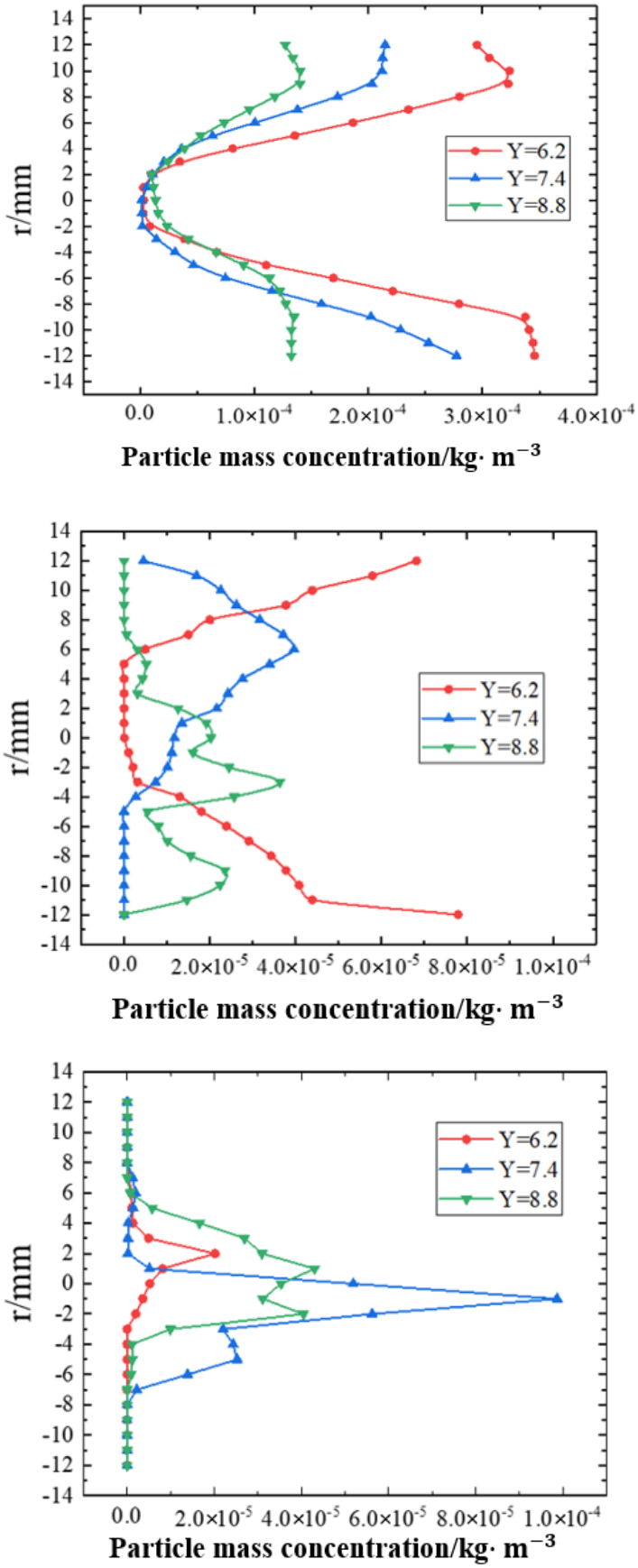

Figure 9. Profiles of particle mass concentration fractions at different positions of the elbow under different twisted rates.

The twisted rate of the swirl-inducing belt significantly affects the distribution of hydrate particles, as shown in Figure 9. The three different positions are the front straight pipe, the 90° bent pipe, and the back straight pipe. Twisted belts generate swirl flow, which disperses particles and prevents their deposition on the pipe walls. At higher twisted rates, the swirl intensity is stronger, leading to more uniform particle dispersion near the walls and a lower mass concentration in the central region of the pipe. As the twisted rate decreases, the tangential velocity imparted by the belt weakens, reducing the effectiveness of the swirl flow. In such cases, particles are more likely to migrate toward the center of the pipe as the flow progresses, resulting in less dispersion and higher localized concentrations. This phenomenon underscores the importance of optimizing the twisted rate to achieve the desired flow characteristics. A smaller twisted rate also ensures that fewer particles remain deposited on the pipe walls, improving the overall transport efficiency and reducing the risk of blockages.

The distance traveled by the particles within the pipeline further influences their residual distribution. As the flow progresses, the tangential forces generated by the swirl flow gradually weaken, allowing gravity and centrifugal forces to take precedence. Over longer flow distances, this decay of swirl intensity leads to a gradual coalescence of particles toward the pipe's centerline. This redistribution has critical implications for pipeline safety and efficiency. For instance, at medium and low flow rates, the reduced swirl intensity is insufficient to overcome gravitational settling, resulting in significant particle deposition along the lower walls of the pipe. This buildup not only increases the likelihood of flow blockages but also reduces the pipeline's effective carrying capacity. Conversely, at higher flow rates, the residual swirl motion and axial velocity are sufficient to carry the particles through the pipeline, minimizing the risk of deposition.

3.4. Hydrate Particle Deposition Laws

In the study of hydrate particle deposition within pipelines, the deposition rate parameter is introduced as a key metric, defined as the percentage of particles deposited per unit of time relative to the number of particles entering the pipeline section in the same timeframe. Mathematically, the deposition rate can be expressed as follows:

$$\varphi = \frac{\mathrm{N_{dep}}}{\mathrm{N_{in}}} \times 100\% \tag{18}$$

where N_{dep} is the number of particles deposited in the pipe; N_{in} is the number of particles entering the pipe.

To evaluate hydrate particle deposition under various conditions, numerical simulations were performed, considering the following influencing factors: bending angle of the pipeline, diameter ratio of the bending pipe, twisted rate of the flow, and Reynolds number. The deposition behavior was analyzed in relation to these parameters, and the resulting variation curves are depicted in Figure 10.

Figure 10a illustrates the correlation between deposition rate, Reynolds number, and twisted rate. The results indicate a sharp decline in the deposition rate as the Reynolds number increases. Specifically, at a Reynolds number of 20,000, the deposition rate drops below 1% for all conditions. This behavior is attributed to the enhanced strength of the swirl flow with increasing Reynolds numbers. Stronger swirl flows counteract the gravitational forces responsible for particle deposition, thus reducing the rate of deposition. Conversely, a decrease in the twisted rate also contributes to a reduction in the deposition rate. This is because a lower twisted rate enhances the helical flow strength within the pipeline, generating shear forces that prevent particles from settling. As a result, under

the combined effect of high Reynolds numbers and low twisted rates, the deposition rate remains minimal.

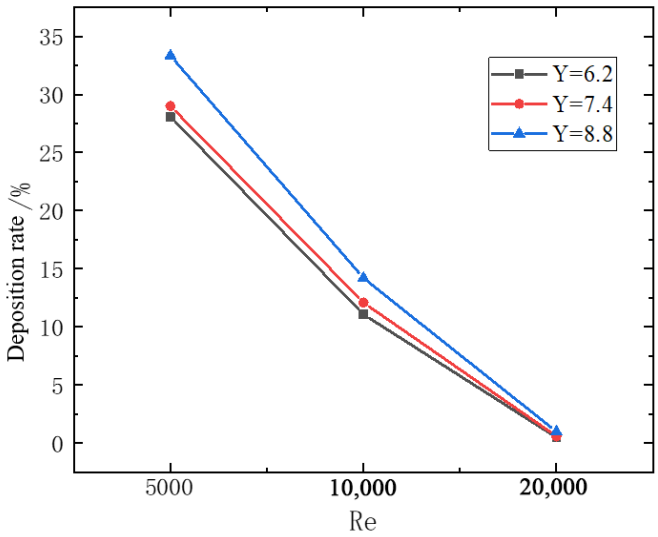

(**a**) Correlation between deposition rate and twisted rate

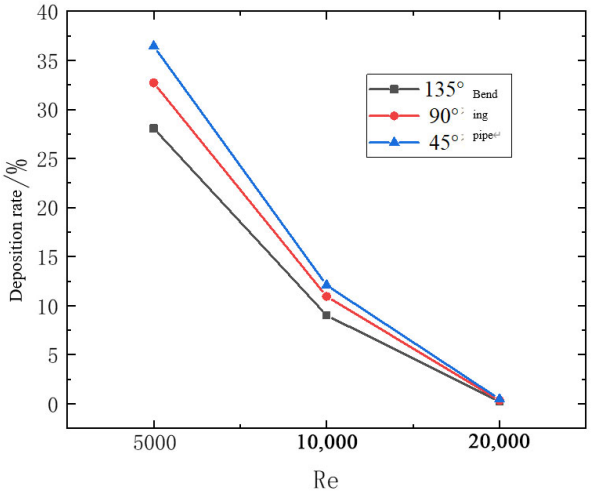

(**b**) Correlation between deposition rate and the bending angle of the pipeline

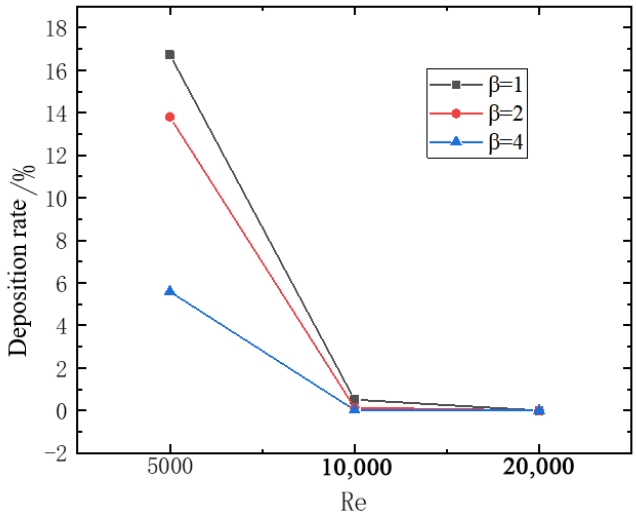

(**c**) Correlation between deposition rate and the bending pipe diameter ratio

Figure 10. Variation curves of particle deposition rate in elbow under different influencing factors.

Figure 10b demonstrates the relationship between the deposition rate and the bending angle of the pipeline. A larger bending angle corresponds to a lower deposition rate. This phenomenon can be explained by the smoother velocity transitions associated with increased bending angles. When the flow traverses a pipe with a larger bending angle, the velocity and swirl strength experience less significant losses, allowing hydrate particles to remain suspended and flow out of the pipeline more effectively. Furthermore, larger bending angles contribute to improved particle dispersion, reducing the tendency of particles to accumulate along the outer wall of the pipe. This minimizes localized deposition and ensures a more uniform distribution of particles within the flow.

Figure 10c highlights the influence of the bending pipe diameter ratio on the deposition rate. An increase in the diameter ratio generally leads to a decrease in the deposition rate. At lower Reynolds numbers, the impact of the diameter ratio is particularly pronounced, with significant differences in deposition rates observed across varying diameter ratios. However, as the Reynolds number rises, these differences gradually diminish. This behavior can be attributed to the geometry of the bending pipe. A higher diameter ratio results in a gentler pipe curvature, which minimizes particle velocity losses and enables a quicker recovery of flow velocity after exiting the bend. Consequently, particles are more likely to remain suspended and flow out of the pipeline, reducing the deposition rate. At lower Reynolds numbers, the fluid's kinetic energy is insufficient to prevent particles from aggregating along the outer wall of the pipe, especially in pipes with smaller diameter ratios. This aggregation reduces the effective flow area, causing sharper velocity changes and greater energy losses. However, at higher Reynolds numbers, the increased flow velocity diminishes the differences in deposition rates caused by variations in the diameter ratio, as particles are carried through the pipeline more efficiently.

4. Conclusions

This study investigates the behavior of gas hydrate particles in bending pipelines under the influence of swirl flow, using numerical simulations to analyze the effects of bending angles, pipe-to-diameter ratios, Reynolds numbers, and twist rates. The findings reveal that larger bending angles and higher Reynolds numbers enhance swirl flow intensity, reducing hydrate particle deposition. A decrease in twist rate helps sustain swirl flow, preventing particle accumulation. The results indicate that optimizing pipeline parameters, such as increasing Reynolds numbers and selecting appropriate bend geometries, effectively minimizes hydrate deposition and ensures safer, more efficient pipeline operations. These insights contribute to the development of improved strategies for gas hydrate transport and pipeline design.

This study has limitations, including the exclusion of pipeline roughness, hydrate particle size variations, and thermal fluctuations. Future research should clarify the interaction between swirl flow and hydrate deposition, particularly transition mechanisms governing particle retention and aggregation. Investigating turbulence, centrifugal forces, and hydrate adhesion will enhance understanding. Experimental validation and advanced multiphase models are crucial for improving predictive accuracy. Addressing these challenges will enable more effective swirl-based flow control strategies, enhancing pipeline reliability and mitigating hydrate deposition. Data availability statement: the data presented in this study are available on request from the corresponding author.

Author Contributions: Conceptualization, Y.R., L.Z., S.W. and C.W.; Methodology, Y.R., W.W., Z.G., S.Z. and C.W.; Formal analysis, L.Z., S.W. and C.W.; Writing—original draft, Y.R. and L.Z.; Writing—review & editing, L.Z., W.W., Z.G., S.Z. and C.W.; Supervision, Y.R., S.W. and C.W. All authors have read and agreed to the published version of the manuscript.

Funding: This research was supported in part by the Key Research and Development Project of Jiangsu Province (No. BE2022001-5), Quanzhou Science and Technology Planning Project (No. 2022N045 and 2024NS004), Open Project of Collaborative Innovation Center for Clean Energy Application Technology (Quanzhou Vocational and Technical University) (No. QJNY22-01), Jiangsu Provincial Graduate Research and Innovation Program Project (No. KYCX24_3245 and SJCX24_1682), and the Engineering and Physical Sciences Research Council [grant number EP/Y022149/1]. For the purpose of open access, the author has applied a 'Creative Commons Attribution (CC BY) license to any Author Accepted Manuscript version arising.

Data Availability Statement: The original contributions presented in this study are included in the article. Further inquiries can be directed to the corresponding author.

Conflicts of Interest: The authors declare no competing interests.

References

1. Basil, N.; Marhoon, H.M. Towards evaluation of the PID criteria based UAVs observation and tracking head within resizable selection by COA algorithm. *Results Control Optim.* **2023**, *12*, 100279. [CrossRef]
2. Basil, N.; Marhoon, H.M.; Gokulakrishnan, S.; Buddhi, D. Jaya optimization algorithm implemented on a new novel design of 6-DOF AUV body: A case study. *Multimed. Tools Appl.* **2022**, *16*, 1–26. [CrossRef]
3. Sloan, E.D.; Koh, C.A. *Clathrate Hydrates of Natural Gases*; Marcel Dekker: New York, NY, USA; Basel, Switzerland; CRC Press: Boca Raton, FL, USA, 2008; pp. 2–5.
4. Lee, J.Y.; Ryu, B.J.; Yun, T.S.; Lee, J.; Cho, G.-C. Review on the gas hydrate development and production as a new energy resource. *KSCE J. Civ. Eng.* **2011**, *15*, 689–696. [CrossRef]
5. Changjun, L.; Ting, H.; Wenlong, J. Deepwater Natural Gas Hydrates and Their Pipeline Transportation Technology. *Chin. Sci. Bull.* **2016**, *61*, 2449–2462.
6. Jing, G.; Hui, S.B.; Xiaofang, L. Hydrate Formation and slurry transportation in multiphase pipeline. *J. China Univ. Pet. Sci.* **2013**, *37*, 163–167.
7. Ding, L.; Shi, B.; Lv, X.; Liu, Y.; Wu, H.; Wang, W.; Gong, J. Hydrate formation and plugging mechanisms in different gas-liquid flow patterns. *Ind. Eng. Chem. Res.* **2017**, *56*, 4173–4184. [CrossRef]
8. Shi, B.-H.; Gong, J.; Sun, C.-Y.; Zhao, J.-K.; Ding, Y.; Chen, G.-J. An inward and outward natural gas hydrates growth shell model considering intrinsic kinetics, mass and heat transfer. *Chem. Eng. J.* **2011**, *171*, 1308–1316. [CrossRef]
9. Wang, S.; Rao, Y.; Hao, C.; Yao, J.; Zhou, S. Numerical Simulation Study on the Influence of Twist Tape Parameters on Hydrate Particle Deposition. *Processes* **2023**, *11*, 1658. [CrossRef]
10. Wen, L.; Sheng, J.; Huazheng, L. Experimental study of liquid-carrying by swirling flow in a U-shaped tube. *Exp. Therm. Fluid Sci.* **2022**, *130*, 110479.
11. Liu, W.; Lv, X.; Zhou, H.; Dou, X. The effect of decay on churn flow transition in a vertical gas-liquid swirling flow. *Chem. Eng. Sci.* **2022**, *259*, 117843. [CrossRef]
12. Al-Obaidi, A.R. Investigation evaluation of thermo-hydraulic flow and heat improvement in a 3D circular corrugated pipe based on response surface method and Taguchi analyses. *Heat Mass Transf.* **2024**, *60*, 573–597. [CrossRef]
13. Xu, R.; Kou, X.; Wu, T.-W.; Li, X.-S.; Wang, Y. Pore-scale experimental investigation of the fluid flow effects on methane hydrate formation. *Energy* **2023**, *271*, 126867. [CrossRef]
14. Sun, H.; Chen, B.; Li, K.; Yang, Y.S.; Jiang, L.; Yan, J. Methane hydrate re-formation and blockage mechanism in a pore-level water-gas flow process. *Energy* **2023**, *263*, 125851. [CrossRef]
15. Sun, H.; Chen, B.; Pang, W.; Song, Y.; Yang, M. Investigation on plugging prediction of multiphase flow in natural gas hydrate sediment with different field scales. *Fuel* **2022**, *325*, 124936. [CrossRef]
16. Sun, H.; Chen, B.; Pang, W.; Yang, Y.S. The enhancement effect of water-gas two-phase flow on depressurization process: Important for gas hydrate production. *Appl. Energy* **2020**, *276*, 115559. [CrossRef]
17. Xiaonan, W.; Qian, L.; Jianyuan, G. Migration of deposited naphthalene particles in urban gas pipelines. *Nat. Gas Ind.* **2019**, *39*, 104–112.
18. Tong, L.; Qiong, H.; Hong, X. Transport characteristics of large particle solid-liquid two-phase flow in U-shaped elbow. *Min. Metall. Eng.* **2019**, *39*, 6–10.
19. Hui, G.; Liejin, G.; Bingqiang, Z. PIV measurement of flow field in liquid film region of gas-liquid-solid three-phase flow in bent pipe. *J. Eng. Thermophys.* **2004**, *2*, 255–258.
20. Elhenawy, S.; Khraisheh, M.; Almomani, F.; Al-Ghouti, M.A.; Hassan, M.K.; Al-Muhtaseb, A. Towards Gas Hydrate-Free Pipelines: A Comprehensive Review of Gas Hydrate Inhibition Techniques. *Energies* **2022**, *15*, 8551. [CrossRef]

21. Ibrahim, A.R.; Basil, N.; Mahdi, M.I. Implementation enhancement of AVR control system within optimization techniques. *Int. J. Nonlinear Anal. Appl.* **2021**, *12*, 2021–2027.
22. Mohammed, A.F.; Basil, N.; Abdulmaged, R.B.; Marhoon, H.M.; Ridha, H.M.; Ma'arif, A.; Suwarno, I. Selection and Evaluation of Robotic Arm based Conveyor Belts (RACBs) Motions: NARMA(L2)-FO(ANFIS)PD-I based Jaya Optimization Algorithm. *Int. J. Robot. Control Syst.* **2024**, *4*, 262–290. [CrossRef]
23. Rao, Y.; Wang, Y.; Wang, S.; Gong, Z.; Zhang, C. Numerical simulation study on the influence of bend diameter rate on the flow characteristics of nature gas hydrate particles. *Sci. Rep.* **2024**, *14*, 31604. [CrossRef] [PubMed]